

A miniaturized magnetic field sensor based on nitrogen-vacancy centers

Stefan Dix,^{1,*} Dennis Lönard,^{1,*} Isabel Cardoso Barbosa,¹ Jonas Gutsche,¹ Jonas Witzenrath,¹ and Artur Widera^{1,†}

¹*Department of Physics and State Research Center OPTIMAS,
University of Kaiserslautern-Landau, Erwin-Schrodinger-Str. 46, 67663 Kaiserslautern, Germany*

(Dated: March 22, 2024)

The nitrogen-vacancy (NV) center in diamond is a prime candidate for quantum sensing technologies. Ongoing miniaturization calls for ever-smaller sensors maintaining good measurement performance. Here, we present a fully integrated mechanically robust fiber-based endoscopic sensor capable of $5.9 \text{ nT}/\sqrt{\text{Hz}}$ magnetic field sensitivity utilizing $15 \text{ }\mu\text{m}$ sized microdiamonds at a microwave power of 50 mW and optical power of 2.15 mW . A direct laser writing process is used to localize a diamond containing NV centers above the fiber's core by a polymer structure. This structure enables stable optical access and independent guiding of excitation and fluorescent light in different optical fibers. This separation strongly reduces the contribution of autofluorescence from the excitation light in the optical fiber. Moreover, a metallic direct laser written antenna structure is created next to the fibers' facet, allowing microwave manipulation of the NV centers' spins. The fabricated endoscopic sensor provides a robust platform with a tip diameter of $1.25 \text{ }\mu\text{m}$. The device enables remote optical and microwave access to perform the full range of coherent spin measurements with NV centers at a spatial resolution of $15 \text{ }\mu\text{m}$. We demonstrate the capability of vector magnetic field measurements in a magnetic field as used in state-of-the-art ultracold quantum gas experiments, opening a potential field in which high resolution and high sensitivity are necessary.

I. INTRODUCTION

The negatively charged nitrogen-vacancy (NV) center in diamond is an atomic-scale point defect in the diamond lattice consisting of a vacancy and a substitutional nitrogen atom next to it [1, 2]. It provides optically addressable spin states and allows optical readout of the spin-state population [3]. When resonantly excited with a microwave (MW) field, it enables, due to spin-dependent intersystem crossing, optically detected magnetic resonance (ODMR) spectroscopy [4]. The inclusion of the defect in the diamond lattice results in a solid-state sensor with atom-like behavior [5], making it a leading candidate in research as a highly sensitive vectorial magnetic field sensor with high spatial resolution [6] and the capability to measure temperature [7, 8], pressure [9], and electrical fields [10–13]. Other magnetic-field sensors such as superconducting quantum interference devices (SQUIDs) and optically pumped atomic magnetometers (OPAMs) have demonstrated sensitivities in the $\text{fT}/\sqrt{\text{Hz}}$ range [14, 15]. However, they often require cryogenic temperatures or are not intrinsically capable of measuring vectorial magnetic fields with a single sensing element. Many applications, like measurements of electrical currents in coils or high-power electronics, paramagnetic materials, or permanent magnetic materials, need to be measured accurately with $\text{nT}/\sqrt{\text{Hz}}$ sensitivities [16–19]. Often, they require only moderate absolute sensitivities, but strongly profit from an increased sensitivity per distance [20–22] or if high sensitivity is necessary can be achieved by

increasing the number of spins and volume [23, 24]. Here, diamonds containing NV centers provide high overall sensitivities and the usability from cryogenic temperatures up to hundreds of $^{\circ}\text{C}$ [25–27] promising to be the next generation of magnetic field sensors.

Moreover, single diamond-based sensors have demonstrated vector magnetometry with a wide dynamic range and high sensitivity [16]. Current state-of-the-art approaches to measuring magnetic fields are based on stationary setups such as wide-field microscopy utilizing diamond plates [28], scanning diamond probes [29], or integrated portable devices [30]. The reported portable devices can be split up into two groups. Either they are fully integrated, consisting of necessary excitation and detection elements such as MW antennas, optical excitation light sources, and detectors close by or directly attached [31–33]. Alternatively, they consist of two parts where the sensor's head, as well as the excitation and detection sections, are separated with optical fibers and electrical wires [34–38]. However, integrating these elements, such as detectors and excitation sources, limits the possible miniaturization of the actual sensor. Therefore, miniaturization can be enhanced by only integrating the necessary elements on a sensor's tip and connecting them to wires and optical fibers. Combining an NV-doped diamond with optical and microwave access on a compact form factor leads to challenges in finding a robust platform. Previously reported results suggest that positioning the microwave emitting element near the diamond can provide a good sensitivity even at low power settings [39].

In this context, an important limitation of miniaturized optical fiber-based sensors is the so-called autofluorescence of optical fibers [40, 41]. This fluorescence arises from the necessary excitation light required for NV centers, which excites photo-active

* Both authors contributed equally

† widera@physik.uni-kl.de

compounds within the fiber and typically overlays spectrally with the fluorescence of the NV center. When the diamond size, respectively the number of NV centers, is decreased, the total fluorescence from the actual sensor decreases while the autofluorescence remains constant for the same laser power. This leads to a lower signal-to-noise (SNR) ratio, hence worse sensitivity, or makes it entirely impossible to measure a weak signal. Although many manufacturers suggest bleaching strategies to reduce the autofluorescence intensity temporarily, it can not be eliminated completely.

Here, we show an approach to reduce autofluorescence by embedding one optical fiber for excitation and one fiber for detection combined with light-guiding structures between both fibers and the diamond. Using this approach, the amount of laser light guided in the detection fiber is reduced by a factor of ≈ 800 . This allows future integration of much smaller diamonds without reducing the SNR compared to single fiber sensors. We demonstrate a magnetic field sensor with a shot noise limited sensitivity of $5.9 \text{ nT}/\sqrt{\text{Hz}}$ and a spatial resolution of $15 \mu\text{m}$ at a microwave power as low as 50 mW and optical laser power of 2.15 mW with a total volume of our sensor head of 52.8 mm^3 . We find a volumetric sensitivity related to our total sensor head size of $42.9 \text{ mm}^3/2 \times \text{nT}/\sqrt{\text{Hz}}$ and volumetric sensitivity related to the diamond size of $7.8 \text{ mm}^3/2 \times \text{pT}/\sqrt{\text{Hz}}$ assuming the microdiamond as a homogeneous $15 \mu\text{m}$ -sized sphere. We use standardized components and state-of-the-art additive manufacturing techniques, such as direct laser writing of silver and polymer structures, and present a new way to miniaturize a fiber-based integrated sensor while maintaining high mechanical stability.

In the following sections, we first describe the steps to create a robust platform, including antenna and optical structures with an integrated $15 \mu\text{m}$ -sized diamond. Section II A describes the steps to create a robust platform containing optical access and electrical channels. Section II B continues with our method to create a magnetic microwave field emitting structure on the tip of the sensor platform next to the facet of two optical fibers. In section II C, we show the method we use to attach a diamond to the tip of an optical fiber and efficiently couple excitation light to the diamond and fluorescence light to a detector. Further, we describe the packaging and last steps of our sensor fabrication, making it practically portable in section II D. In section III, we describe our measurement setup and subsequently characterize our sensor in terms of autofluorescence, sensitivity, and noise, and show a practical application in section IV.

II. MATERIALS AND METHODS

Our sensor head is split into two components, the so-called sensor platform and the tip of the sensor. The sensor platform connects the MW guiding wires and light

guiding optical fibers together in an optical fiber ferrule with an inner diameter of $270 \mu\text{m}$ as depicted in FIG. 1 (A). After filling the remaining space using epoxy and subsequent polishing of the tip, the small tip diameter enables the use of microscopic additive technologies such as direct laser writing at the tip of the fibers and wires as shown in FIG. 1 (B-D).

The platform also enhances the mechanical stability of the whole sensor without significantly increasing the size of the necessary parts of the sensor. The tip of the sensor contains two direct laser written structures whereof one is a silver antenna structure and one is a light guiding structure connecting two optical fibers. Additionally, an NV-doped ($\approx 3.5 \text{ ppm}$) $15 \mu\text{m}$ -sized microdiamond (MDNV15umHi, Adamas Nanotechnologies) is fastened to the sensor tip inside the DLW structure. For the fabrication of the polymer and silver structure on the sensor's tip, we employ direct laser writing processes using a Nanoscribe-System (PPGT+). In these processes, the polished tip is either positioned in silver resist or in photoresist (IP-Visio, Nanoscribe) above a glass coverslip and the microscope objective of the Nanoscribe system. We utilize a combination of XYZ stages and a rotatable fiber tip holder connected on top of the motorized XY stage of the Nanoscribe system to precisely position the sensors' tip above the objective using the camera of the device. In the last step, the sensor platform is packaged into an optional, rigid hollow rod, and the scattering parameters of the antenna are tuned. A detailed description of all steps of the fabrication is given in the following subsections.

A. Sensor platform

For the fabrication of the sensor platform, we use two optical fibers with a cladding diameter of $125 \mu\text{m}$ (FG050LGA and 460HP, Thorlabs) and two silver wires (99.9% silver) with outer diameters of $100 \mu\text{m}$. Wires and fibers are inserted in a ceramic ferrule for optical fibers with an inner diameter of $270 \mu\text{m}$ and an outer diameter of 1.25 mm (CFX270-10, Thorlabs), as depicted in FIG. 1 (A). The diameters of the fibers and wires are specifically chosen such that they tightly fit in the ceramic ferrule, ensuring repeatable arrangement and dimensions for the fabrication of the silver antenna and light-guiding structures, as shown in FIG. 1 (B) and (D). Furthermore, the fibers and wires are jacketed with flexible, protective tubing for optical fibers with an outer diameter of 0.9 mm (FT900KB and FT900KK, Thorlabs). As an assembly adapter, a finely machined metal or polycarbonate sleeve connects the ceramic ferrule and the tubing. All elements of the sensor platform are then fixed in position using epoxy (353NDPK, Thorlabs). After curing the epoxy at 80°C for 1 h, the tip of the sensor platform is polished using optical fiber polishing tools.

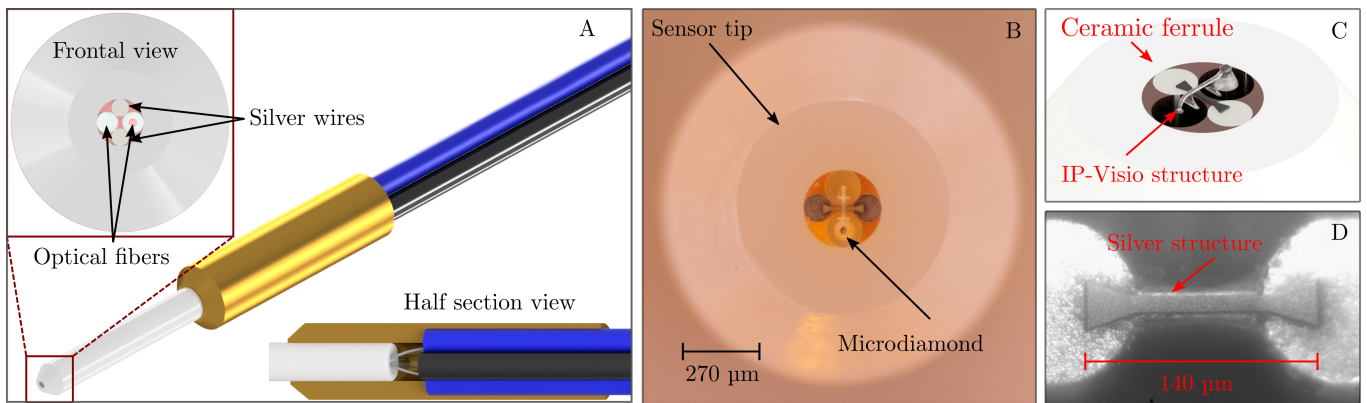


FIG. 1. (A) rendered images of the assembled sensor platform. Two silver wires and two optical fibers are inserted into a ceramic ferrule. As a reinforcement between the ferrule and the protective tubing of the fibers a mating sleeve is added. (B) tip of a sensor after fabrication without galvanisation. (C) rendered view of the processed tip. (D) microscopic image of the direct laser written silver structure connected to the silver wires.

B. Antenna fabrication

The antenna, consisting of elemental silver, is created using a metallic direct laser writing process. First, the fiber tip is positioned in a small reservoir filled with a silver resist, which encompasses the sensors' tip and is placed above the glass substrate, eliminating evaporation issues with the water-based silver solution. Using a 2D silver resist [39, 42] and a 20x 0.5 NA objective (EC Epiplan-Neofluar, Zeiss), we directly write a silver microstrip-like antenna as shown in FIG. 1 (D), which can already be used to excite the microwave transitions of NV centers without further processing. Optionally, a subsequent galvanization step can be conducted after the silver DLW process, which increases the efficiency of the MW emission and lowers the ohmic resistance of the antenna by approximately one order of magnitude. For this, a silver wire (99.99%) with a diameter of $200\ \mu\text{m}$ is wound around the sensor tip to serve as an anode. For the sensor shown in FIG. 2 we galvanized the structure for 2 min at 0.7 V using a commercial silver solution, which reduced the ohmic resistance from $\approx (35.0 \pm 0.5)\ \Omega$ to $\approx (3.3 \pm 0.5)\ \Omega$ when measured at the SMA (SubMiniature version A) connector.

C. Optical structure and diamond connection

In order to connect a diamond containing NV centers to an optical fiber, the tip of the multi-mode (MM) fiber is positioned $50\ \mu\text{m}$ above the diamond using the microscope of the Nanoscribe system. We use a polymer resist (IP Visio), which provides a low fluorescence and high optical transparency in the visible spectrum [43]. As a connecting and light-guiding element, a cone structure is direct laser written between the core of the MM fiber and the diamond. The base of the cone is adapted to the size of the core of the MM fiber, and the tip of the

cone is designed to be slightly larger than the diamond. Due to the scattering of the laser beam in the center of the cone caused by the microdiamond, the structure is written hollow using only contour lines. A second polymer structure is written between a single-mode (SM) fiber and the diamond to connect the SM fiber to the diamond for an additional optical excitation beam path. It is shaped such that optical excitation light hits the diamond from the side, reducing the overall excitation light in the MM fiber. Further details can be found in Appendix C. The written structure is post-cured using a UV LED after the chemical development.

D. Resonance tuning, assembly, and packaging

As a last step, the sensor is mounted in an optional metallic or plastic tube with a 5 mm outer and 3 mm inner diameter to enhance the mechanical stability as shown in FIG. 2 (A). A small protective cap can be added around the tip and the ceramic ferrule. The antenna's resonance is tuned by measuring the S_{11} parameter and iterative shortening of the silver wires until a resonance of the S_{11} parameter is measured at (2.8 ± 0.2) GHz. An additional optional cap can be attached to the tip, housing small permanent magnets with a diameter of 1.5 mm and 0.5 mm thickness to achieve a bias magnetic field when small magnetic field shifts need to be measured. An image of the assembled sensor is shown in FIG. 2 (B). The distance between the MW connector and the tip is $\approx 35\ \text{cm}$ while the optical fibers have a length of $\approx 1.7\ \text{m}$ making it an easy-to-mount-and-hold but flexible sensor.

III. MEASUREMENT SETUP

We characterize our sensor by measuring fluorescence characteristics as well as ODMR spectra and their noise

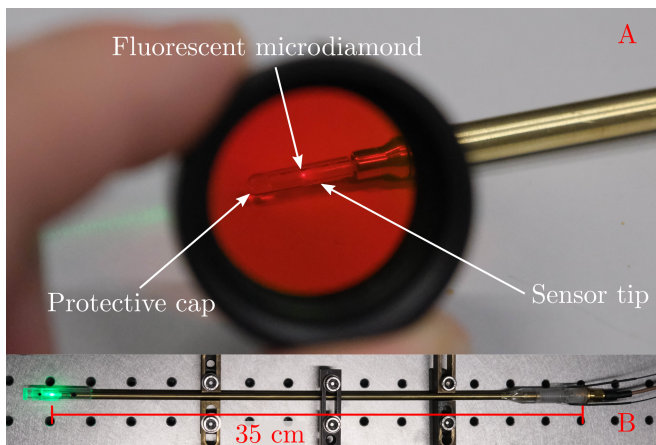


FIG. 2. Images of the assembled sensor with a total length of ≈ 35 cm. (A) close view of the sensor tip encased in a brass rod with a protective cap. The fluorescence of the diamond during excitation through the multimode fiber is shown through a longpass filter (> 600 nm). (B) entire sensor, including the additional optional cap for a constant magnetic bias field, the optical fibers, and the SMA connector for the MW signal connection at the back of the sensor.

fluctuations with the setup shown in FIG. 3. Our optical setup consists of a modular compact enclosure with a size of $215 \times 150 \times 58$ mm³ which contains all necessary optical elements as well as some optional elements to connect an excitation laser, fiber-sensor, and various detectors. A fiber-coupled laser (Cobolt 06-MLD, Hübner Photonics) with a wavelength of 520 nm is used to excite the NV centers optically. To avoid damaging the sensor head through excessive heating, we limit the laser power to 2.2 mW in the following measurements. The laser light is directly coupled into the enclosure, where first a half-wave plate (WPH05ME-514, Thorlabs) and a polarizing beam cube (PBS121, Thorlabs) ensure a linear polarization of the in-coupled laser light. The reflected part of the beam can be monitored by a photodiode (PD) and enables measuring changes in power caused by fluctuations in the polarization. A second non-polarizing beam cube (BS040, Thorlabs) allows monitoring of the optical excitation power and can be used for further improvements using balanced detection schemes. ND filters and laser clean-up filters can be inserted if needed before the laser light is coupled into the sensor head fiber. The collected fluorescence is either separated by a dichroic mirror (SP 69-191, Edmund Optics) for single fiber measurements or, for dual fiber measurements, fluorescence collected from the sensor head is guided back through the second fiber into the optical setup and then filtered with a longpass filter (FELH650, Thorlabs) and further optional ND filters. Finally, the fluorescence intensity is either measured by a photodiode (SM05PD3A, Thorlabs) or an avalanche photodiode (APD) (APD130A, Thorlabs) or coupled to a multimode fiber (M43L05, Thorlabs) which guides the fluorescence light to a single photon counting module

(SPCM) (COUNT-T-100-FC, LaserComponents).

The MW signal used is first generated by a radio-frequency generator (SMB100A, Rohde&Schwarz) and then further amplified by an amplifier (ZHL-16W-43-S+, Mini-Circuits) by 46 dBm. We limit the MW power in the following measurements to ≈ 50 mW to avoid thermally damaging the sensor head. However, we see significant broadening of the ODMR linewidths, indicating that our sensitivity is not limited by the MW power. A coaxial isolator (JIC2700T3500S2, JQL Technologies) is inserted to avoid back reflections before the MW signal is guided via the SMA connector to the fiber head antenna. To determine the actual microwave power at the sensor, we measure the absolute gain between the MW signal generator and the SMA connector of the sensor with a vector network analyzer (MS2038C, Anritsu). We obtain an absolute amplification of the signal in combination with all loss elements (circulator, amplifier, connectors, and connecting cable) of 38 dB.

To perform lock-in amplification of the measured PD/APD signal, we sine-wave modulate the MW frequency. The required reference signal is generated by an arbitrary waveform generator (33622A, Keysight). The PD/APD signal is AC coupled, using a 100 nF capacitance in series, to a lock-in amplifier (LIA) (MFLI 500 kHz, Zurich Instruments), which demodulates and filters the signal. We apply a 3rd order low-pass filter with a 1 ms time constant (equivalent to a 3 dB bandwidth of 80.9 Hz or a noise-equivalent power bandwidth of 93.5 Hz) with the LIA. The phase shift between the reference signal and the measured fluorescence signal is always chosen to maximize the signal of the X component.

All devices are connected to the same 10 MHz clock reference signal. Appendix B contains a more detailed discussion about optimizing individual measurement parameters.

IV. RESULTS

A. Fluorescence measurements

Before characterizing the sensitivity of our sensor, we measure its relevant fluorescence properties and characterize the potential reduction of the autofluorescence. For this purpose, we compare the fluorescence light intensity of an identical unprocessed commercial MM fiber (M42L02, Thorlabs) to the fluorescence from the diamond on the processed MM fiber at the same laser power, wavelength, and same type of fiber. Precisely, we measure the total counts in the relevant fluorescence spectrum using a single photon counting module (SPCM), neutral density (ND) filters, and a longpass filter with a cutoff wavelength of 650 nm at an excitation laser power of 2.2 mW and compare the detected fluorescence counts, which are normalized by the coupling efficiency. The absolute

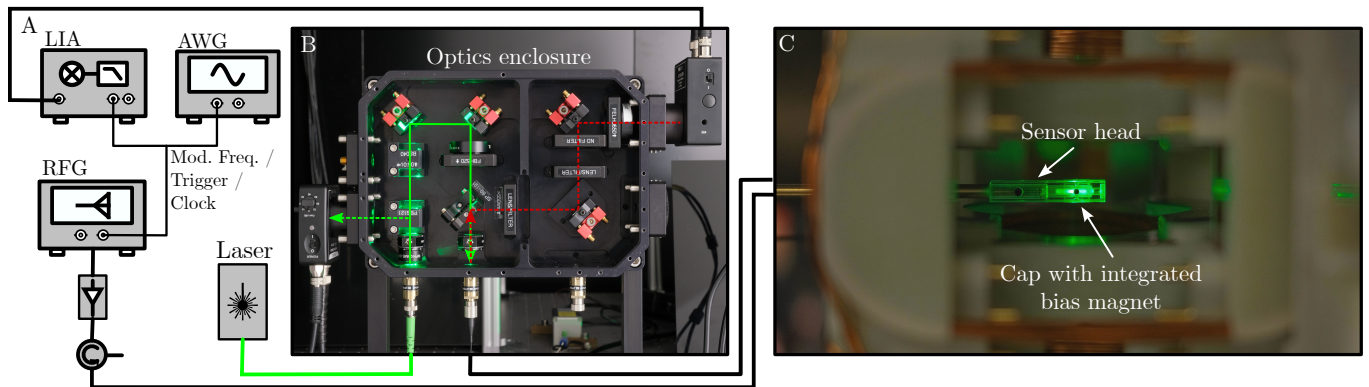


FIG. 3. Schematics of the electrical and optical setup, specifically in a configuration for LIA measurements. (A) The MW signal is frequency modulated and directly connected to the sensor. The fluorescence signal, measured either with a PD or an APD, is demodulated and filtered by a LIA. (B) Optical fiber coupling is done in a custom anodised enclosure, milled from aluminium. A first half-wave plate and a polarizing beam cube ensure a linear polarization of the in-coupled laser light and allow monitoring changes in laser power caused by fluctuations in the polarization via a PD. A second non-polarizing beam cube allows monitoring of the optical excitation power and can be used for further improvements using balanced detection schemes. ND and laser clean-up filters can be inserted, if needed, before the laser light is coupled into the sensor head fiber. The collected fluorescence is either separated by a dichroic mirror for single fiber measurements or, for dual fiber measurements, fluorescence collected from the sensor head is guided back through the second fiber into the optical setup and then filtered with a longpass filter. Finally, the fluorescence intensity is either measured by a PD or an APD or coupled to a MM fiber which guides the fluorescence light to a SPCM. (C) The sensor head inside of the coil system. A bias magnetic field can be applied with a screw-on cap containing an integrated magnet.

count rate is calculated by applying correction factors for each ND filter at the given transmission value at a wavelength of 685 nm, which is close to the NV center’s maximum emission wavelength of 684 nm at room temperature [44]. We detect a light signal of 3.9×10^8 cps (counts per second) from the commercial MM fiber and 3.3×10^{12} cps of fluorescence light from the 15 μm sized diamond through the sensors’ MM fiber. This yields a contrast ratio of $\approx \frac{8410}{1}$ from which we estimate the minimal diamond size necessary to have a contrast ratio SNR = 1. From this, we find a minimum size of 740 nm when assuming a constant homogeneous laser power, the same optical fiber configuration, and a constant NV doping. Next, we measure the transmitted light through both sensor fibers when exciting the diamond via the SM fiber and detecting it through the sensor’s MM fiber. We detect a transmitted laser power of 2.04 μW compared to an excitation power of 1.64 mW and thus find a reduction of the laser light in the detection fiber by a factor of 804. This theoretically allows the integration of much smaller diamonds on the tip of a fiber down to a size of 79 nm and the same NV-doping of (≈ 3.5 ppm). Assuming a linear scaling of the autofluorescence using the exact same methods as shown before, this would lead to even higher spatial resolutions in the same sensor package. Furthermore, we measure a reduction in the fluorescence intensity by a factor of only 9.9 using this excitation and detection setup. We attribute this reduction of fluorescence intensity to a reduced laser coupling efficiency to the SM fiber and imperfect waveguide geometry, possibly due to manufacturing tolerances and the slightly worse

coupling efficiency into the single-mode fiber. Although this approach effectively overcomes elementary issues associated with smaller diamonds, direct excitation and detection through the same MM fiber results in ten times higher fluorescence for larger diamonds in our case, which mainly results from a lower optical excitation power. Consequently, we archive better sensitivities due to only a slight impact on the SNR when utilizing a 15 μm sized diamond. Therefore, in the following, knowing that our SNR is only moderately reduced at this diamond size, we use the sensors’ MM fiber for excitation and detection if it is not stated otherwise. For smaller diamonds, however, physical separation of the light path for excitation and detection yields significant advantages.

B. Sensitivity characterization

Sweeping over a range of MW frequencies results in an ODMR spectrum of the NV resonances, as shown in FIG. 4. We track the X component of the LIA output over time, and the MW frequencies are calculated via the sweeping time.

An unconstrained non-linear least squares fit method (Levenberg-Marquardt) [45] is used to fit a model function of a sum of the derivatives of eight Lorentzian distributions

$$L(f) = \sum_{i=1}^8 -\frac{32}{3\sqrt{3}} \frac{C_i w_i^3 (f - f_i)}{(4(f - f_i)^2 + w_i^2)^2}, \quad (1)$$

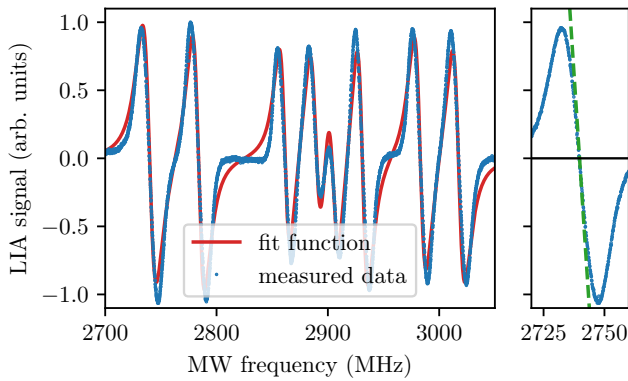


FIG. 4. Left: Lock-in amplified ODMR signal while a bias magnetic field is applied (solid blue). Resonances are fitted with derivatives of Lorentzian functions (red), where the zero-crossing marks the resonance frequency. Right: Magnetic field sensitivity is dependent on the slope at the zero-crossing point (dashed green) for each resonance.

where for the i -th resonance ($i \in (1, \dots, 8)$) C_i is the peak contrast, defined as the maximum value, f_i is the resonance frequency, and w_i is the FWHM linewidth. We found that to automate the selection of starting points for the fit model, using the mean abscissas between the peaks and valleys for each resonance frequency leads to reasonably stable fitting behavior.

The achieved magnetic field sensitivity is highest at the zero-crossing point, where the fit function has a maximal slope S_i . A small change in the external magnetic field along the NV-axis will shift the resonances by the gyromagnetic ratio $\gamma = g_e \mu_B / h \approx 28.03 \text{ GHz T}^{-1}$ of the NV center [3]. The output of the LIA will then react with a change of output voltage at the previous resonance frequency of magnitude

$$R_i = \gamma S_i = \frac{32\sqrt{3}}{9} \frac{g_e \mu_B}{h} \frac{C_i}{w_i}, \quad (2)$$

where R is called the magnetometer response. The magnetic field sensitivity, defined as the minimal change of magnetic field δB that can be resolved in a given time t , is related to the standard deviation of the LIA output σ , the magnetometer response R and the noise-equivalent power (NEP) bandwidth of the LIA's low-pass filter f_{NEP} [46]

$$\eta_{\text{LIA}} = \delta B \sqrt{t} = \frac{\sigma}{R \sqrt{2f_{\text{NEP}}}} \left[\text{T}/\sqrt{\text{Hz}} \right]. \quad (3)$$

We reach an optimal sensitivity of $51.8 \text{ nT}/\sqrt{\text{Hz}}$ for one continuous ODMR sweep for a MW power of 50 mW and laser power of 2.15 mW. A more detailed discussion about optimizing measurement parameters can be found in Appendix B.

To estimate the photon shot noise limit, we average over multiple ODMR measurements with a SPCM at the

same MW and laser powers and calculate the shot noise limited sensitivity for each axis according to [47]

$$\eta_{\text{SN}} = \frac{4}{3\sqrt{3}} \frac{h}{g_e \mu_B} \frac{w}{C \sqrt{I_0}} \left[\text{T}/\sqrt{\text{Hz}} \right], \quad (4)$$

where I_0 is the photon collection rate, corrected for optical losses due to the filters and the detectors efficiency. The most optimal shot-noise limited sensitivity for one resonance is $5.9 \text{ nT}/\sqrt{\text{Hz}}$. To test our two-fiber scheme for reducing the impact of fiber autofluorescence, we compare the sensitivity to an otherwise identical measurement but excite the NV centers via the SM fiber and still detect the signal using the MM fiber. The ODMR spectra, in which we optically excite the NV centers via the MM and SM fiber, are shown in FIG. 5. The sensitivity of all NV axes is listed in Tab. I. The best sensitivity of our sensor is achieved when exciting and detecting through the MM fiber ($5.9 \text{ nT}/\sqrt{\text{Hz}}$) compared to the identical measurement with excitation through the SM fiber ($27.7 \text{ nT}/\sqrt{\text{Hz}}$). We attribute this decrease in sensitivity to a reduced fluorescence due to a lack of optical excitation power from the SM fiber and MW-induced power broadening of the linewidth. Normalizing the sensitivity with respect to the volume of the diamond enables comparability with other sensors and, thus, the characterization of the efficiency of the sensor platform independent of the size of the diamond. Therefore, we multiply the sensitivity by the square root of the diamond size or the sensor volume, as the sensitivity increases with the square root of the number of emitting spins. The volumetric sensitivity related to our total sensor head size is $42.9 \text{ mm}^{3/2} \times \text{nT}/\sqrt{\text{Hz}}$ and the volumetric sensitivity related to the diamond size is $7.8 \text{ mm}^{3/2} \times \text{pT}/\sqrt{\text{Hz}}$ assuming a homogeneous $15 \mu\text{m}$ -sized sphere for the diamond.

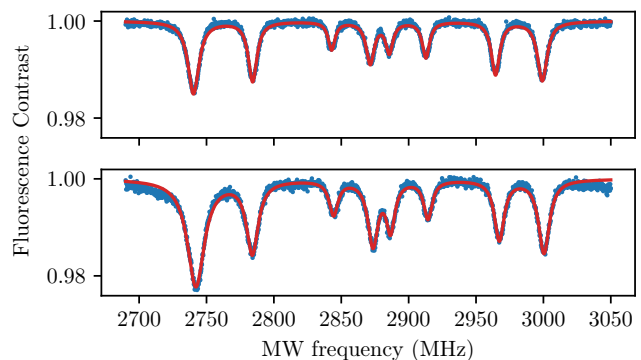


FIG. 5. The upper graph shows the ODMR spectrum, when exciting and detecting via the MM fiber of the sensor. The lower graph shows the ODMR spectrum, when exciting via the SM fiber and detecting through the MM fiber. Resonances are fitted with Lorentzian functions (red) to obtain contrast and linewidth.

C. Noise floor

Next, we characterize the noise floor of our sensor by keeping the MW excitation frequency fixed to one resonance and evaluating the amplitude spectral noise density (SND) [30, 48, 49] and the overlapping Allan deviation [50].

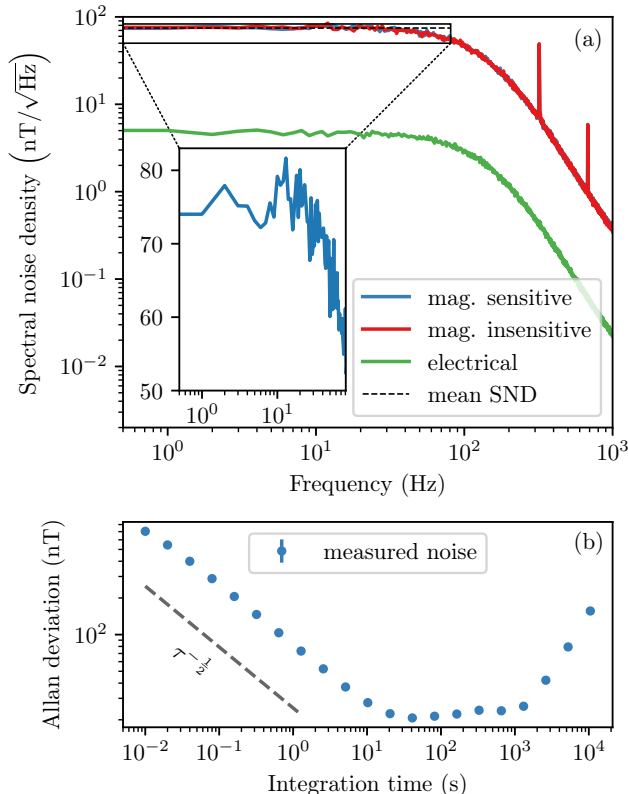


FIG. 6. (a) Amplitude spectral noise density of our sensor for magnetically sensitive (blue), magnetically insensitive (red), and electrical (green) noise measurements. We reach a mean spectral noise density of $74.6 \text{ nT}/\sqrt{\text{Hz}}$ (dashed black) in a 3dB bandwidth of 80.9 Hz. (b) Overlapping Allan deviation of our sensor. Errorbars for the Allan deviation are too small to be visible.

For the SND, the resulting signal is binned into windows of 1 s duration each. We then calculate the absolute value of the averaged single-sided discrete Fourier transform $|\mathcal{F}|$ of the signal. The SND follows from the relation [34, 51]

$$\text{SND} = \frac{|\mathcal{F}|}{R} \sqrt{\tau} \left[\text{T}/\sqrt{\text{Hz}} \right], \quad (5)$$

where the Fourier transform is scaled by the magnetometer response R and the single-sided bandwidth $1/\tau$ of the rectangle window function, which results from the binning of the discrete Fourier transform. The bandwidth scaling is proportional to $\sqrt{\tau}$, because we consider the amplitude SND, which is

the square-root of the power SND. We note that in some literature amplitude is defined as root-mean squared amplitude [51, 52], leading to a scaling difference of $1/\sqrt{2}$ in SND. When recording the X component of the LIA output signal, the signal is said to be magnetically sensitive, while recording the Y component, which is not dependent on magnetic field changes, denotes the magnetically insensitive case. Additionally, we measure the noise without laser excitation, resulting in only electrical noise from the PD and the LIA [34]. FIG. 6 shows the SND for all three cases. We notice uncanceled noise peaks at multiples of ≈ 300 Hz. Because these peaks appear in both magnetically sensitive and insensitive cases, we attribute this noise to our laser. In the future, we plan to employ balanced-photo detection schemes [46] to further mitigate laser noise.

The bandwidth of our sensor is limited by the 3 dB bandwidth of the low-pass filter of our LIA to 80.9 Hz, as indicated by the inset in FIG. 6 (a). We reach a mean SND of $74.6 \text{ nT}/\sqrt{\text{Hz}}$ in this bandwidth. When AC magnetic fields with higher bandwidths are to be recorded, the bandwidth of our sensor can trivially be extended up to the modulation frequency of the LIA. The modulation frequency can then also be further extended to higher frequencies [46]. However, a trade-off between modulation frequency and sensitivity is then necessary, as discussed in Appendix B.

To characterize the long-term stability of our sensor, we record a data set for a longer time of ≈ 15 h and calculate its overlapping Allan deviation. We reach a minimal sensitivity of 21.3 nT for an integration time of 41 s as shown in FIG. 6 (b). We conclude, that the integration of optical fibers, MW antenna, and the NV doped diamond in a fixed package on our sensor head results in a highly stable sensor platform, that is capable of resolving magnetic fields down to the nT range.

D. Magnetic field measurements

We demonstrate a magnetic field measurement of an Anti-Helmholtz coil system to illustrate the real-world benefits that NV-based sensors bring over conventional solutions like Hall sensors. The intrinsic vectorial resolution of our sensor allows us to measure the direction of the magnetic field directly in a single measurement without the need to measure in multiple directions compared to a Hall sensor with a single Hall element. For this, our sensor is fastened to a stage and moved in three dimensions through the magnetic field, and a screw-on cap with integrated permanent magnets is fixed to the tip of our sensor to apply a bias magnetic field of 10.3 mT as depicted in FIG. 3. Triangle-shaped sweeps were performed to mitigate the influence of delays between the sweep and the data recording, and the following resonance frequency calculations are always averaged between one up-scan and one down-scan. We then calculate the absolute value of the magnetic field vector

B for each NV-axis j from its upper and lower resonance frequencies $f_{u,j}$ and $f_{l,j}$ according to (see Appendix A)

$$B = \gamma \frac{1}{4} \sum_{j=1}^4 |B_j|, \quad (6)$$

$$B_j^2 = \frac{1}{3} (f_{u,j}^2 + f_{l,j}^2 + f_{u,j}f_{l,j} - D^2 - 3E^2). \quad (7)$$

$D = 2.87$ GHz denotes the zero-field splitting and $E \approx 5$ MHz is the diamond dependent stress-splitting. The angles θ_j between the magnetic field vector and each NV axis are determined by

$$\cos^2 \theta_j = \frac{-2f_{l,j}^3 + 3f_{l,j}^2 f_{u,j} + 3f_{l,j} f_{u,j}^2 - 2f_{u,j}^3}{27(D-E)B^2} + \frac{2D^3 + 18DE^2}{27(D-E)B^2} + \frac{D-3E}{3(D-E)} \quad (8)$$

and the final magnetic field vector is calculated as

$$\vec{B} = \gamma B \frac{\sqrt{3}}{4} \begin{pmatrix} 1 & -1 & -1 & 1 \\ 1 & -1 & 1 & -1 \\ 1 & 1 & -1 & -1 \end{pmatrix} \cdot \begin{pmatrix} \cos \theta_1 \\ \cos \theta_2 \\ \cos \theta_3 \\ \cos \theta_4 \end{pmatrix}. \quad (9)$$

To calibrate the sensor with the applied bias field, we calculate one magnetic field vector without a coil magnetic field. This bias field is then subtracted from subsequent measured field vectors. FIG. 7 shows one scan of magnetic field vectors in one xy -plane inside the coil system.

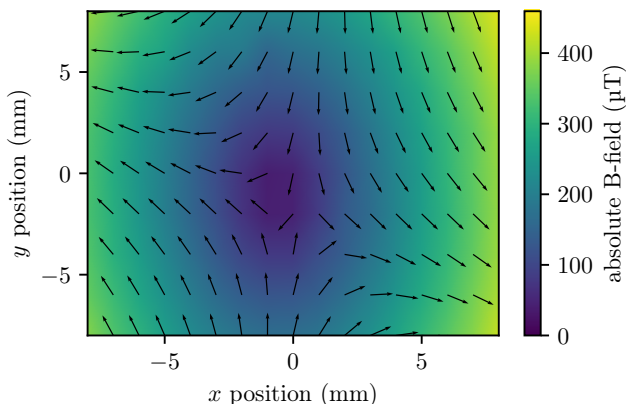


FIG. 7. Contour plot of the measured Helmholtz coil magnetic field in Anti-Helmholtz configuration. Absolute field values are shown as a colorbar. x and y components of the field vector are shown as black arrows.

V. CONCLUSION AND OUTLOOK

The miniaturized fiber-based sensor we present here provides a small sensor platform capable of measuring

magnetic fields in full vectorial resolution. The direct laser writing of polymer and silver structures onto the sensor's tip enables us to fully integrate the diamond and a microwave antenna onto the sensor head. When analyzing the fluorescence properties of our sensor, we find that with our approach, we can reduce the amount of autofluorescence in the detecting fiber by a factor of ≈ 800 and, thus enabling the integration of even smaller diamonds with only a small impact to the SNR. Together with a diamond size, and thus spatial resolution, of $15 \mu\text{m}$, we have demonstrated a highly sensitive, small, and robust sensor platform and show an integrated fiberized NV-based sensor with the smallest diamond size published to date. We achieve a shot-noise limited sensitivity of $5.9 \text{ nT}/\sqrt{\text{Hz}}$, while only using 2.15 mW of laser power and 50 mW of microwave power. The sensitivity of the sensor using lock-in-amplification techniques is $51.8 \text{ nT}/\sqrt{\text{Hz}}$ at the same powers. Using this platform, we are able to integrate ever-smaller diamonds down to a size below 100 nm , overcoming autofluorescence limits of single fiber-based sensors, potentially leading to magnetic field maps with extremely high spatial resolutions. Using this technique, we show, as a practical use case, the measurement of vectorial magnetic fields of a coil system. Furthermore, we emphasize that our approach shows that reducing the total sensor size can achieve high sensitivities at low laser and microwave powers, enabling light and microwave-sensitive measurements.

VI. DATA AND CODE AVAILABILITY

All data shown in the images, plots and data supporting the findings in this publication is available on Zenodo [53]. The code library used to control the devices for all measurements can be found in [54].

VII. ACKNOWLEDGEMENTS

We acknowledge support by the nano-structuring center NSC. This project was funded by the Deutsche Forschungsgemeinschaft (DFG, German Research Foundation) Project-ID No. 454931666 and the Quanten-Initiative Rheinland-Pfalz (QUIP). Furthermore, we thank Dr. Erik Hagen Waller for providing the silver resist as well as Prof. Dr. Georg v. Freymann, Prof. Dr. Elke Neu-Ruffing, Alexander Bukschat, Nimba Pandey, Oliver Opaluch and Tobias Pätkau from the University of Kaiserslautern-Landau for helpful discussions and experimental support. We also thank Dr. Gesa Welker and Dr. Samer Kurdi from the van der Sar Lab at TU Delft for their support on technical questions.

Appendix A: Magnetic field calculation

To calculate the magnetic field from measured resonances, we solve the NV-Hamiltonian analytically, following [55]. Consider the shifted Hamiltonian for one NV center [3] with $\text{Tr}(H) = 0$

$$H = DS_z^2 + E(S_x^2 + S_y^2) + \frac{\vec{B}}{\gamma} \cdot \vec{S} - \frac{2}{3}DI, \quad (\text{A1})$$

where $D = 2.87$ GHz is the zero-field splitting, $E \approx 5$ MHz is the diamond dependent stress-splitting, \vec{B} is the magnetic field vector, $S_{x,y,z}$ are the 3×3 Pauli matrices and I is the unit matrix. Without loss of generality, the magnetic field $\vec{B} = \gamma B(\sin \theta \hat{x} + \cos \theta \hat{z})$ can always be rotated around the NV-axis to remove the B_y component, where θ is the angle between the magnetic field vector and the NV-axis. The roots of the characteristic polynomial are then given by

$$0 = \lambda^3 - \left(\frac{1}{3}D^2 + E^2 + B^2\right)\lambda - \frac{1}{2}DB^2 \cos(2\theta) - EB^2 \sin^2 \theta - \frac{1}{6}DB^2 + \frac{2}{27}D^3 - \frac{2}{3}DE^2. \quad (\text{A2})$$

This polynomial has three real roots λ_1 , λ_2 and λ_3

$$(\lambda - \lambda_1)(\lambda - \lambda_2)(\lambda - \lambda_3) = \lambda^3 - (\lambda_1 + \lambda_2 + \lambda_3)\lambda^2 + (\lambda_1\lambda_2 + \lambda_2\lambda_3 + \lambda_1\lambda_3)\lambda - \lambda_1\lambda_2\lambda_3. \quad (\text{A3})$$

When defining upper and lower resonance frequencies as $f_u = \lambda_3 - \lambda_1$ and $f_l = \lambda_2 - \lambda_1$, these roots can be expressed as $\lambda_1 = (-f_u - f_l)/3$, $\lambda_2 = (2f_l - f_u)/3$ and $\lambda_3 = (2f_u - f_l)/3$ respectively.

We compare the individual terms of Equ. A2 and A3 to derive formulas for B^2 and $\cos^2 \theta$. Comparing linear terms leads to

$$B^2 = \frac{1}{3}(f_u^2 + f_l^2 + f_u f_l - D^2 - 3E^2), \quad (\text{A4})$$

while comparing constant terms leads to

$$\cos^2 \theta = \frac{-2f_l^3 + 3f_l^2 f_u + 3f_l f_u^2 - 2f_u^3}{27(D - E)B^2} + \frac{2D^3 + 18DE^2}{27(D - E)B^2} + \frac{D - 3E}{3(D - E)}. \quad (\text{A5})$$

After measuring both resonance frequencies $f_{u,j}$ and $f_{l,j}$ for all four NV-orientations j , Equ. A4 gives us four independent measurements of the absolute value of the magnetic field. We can simply take the mean value of all four B_j as our final result B .

We now only know the angles θ_j between the magnetic field vector and the NV-axis j . This is akin to four cones in three-dimensional space, where we want to find

the vector that best overlaps all four cones [56]. The magnetic field direction can be obtained by considering the scalar product $\hat{n} \cdot \hat{b} = \cos \theta$ between the NV-axis unit vector \hat{n} and the magnetic field unit vector \hat{b} . This gives us a linear over-determined system $Nb = c$ of four equations with three unknowns that can be written in matrix form as

$$\frac{1}{\sqrt{3}} \begin{pmatrix} 1 & 1 & 1 \\ 1 & -1 & -1 \\ -1 & 1 & -1 \\ -1 & -1 & 1 \end{pmatrix} \cdot \begin{pmatrix} b_x \\ b_y \\ b_z \end{pmatrix} = \begin{pmatrix} \cos \theta_1 \\ \cos \theta_2 \\ \cos \theta_3 \\ \cos \theta_4 \end{pmatrix}, \quad (\text{A6})$$

where the matrix N is constituted of the unit vectors along the NV-axes, which are parallel to $[111]$, $[\bar{1}\bar{1}\bar{1}]$, $[\bar{1}1\bar{1}]$ and $[\bar{1}\bar{1}1]$ respectively [46].

The solution to this kind of linear least-square problem is known to be $\hat{b} = (N^T N)^{-1} N^T c$ [57], which gives us our final magnetic field vector $\vec{B} = \gamma B \hat{b}$ as

$$\vec{B} = \gamma B \frac{\sqrt{3}}{4} \begin{pmatrix} 1 & -1 & -1 & 1 \\ 1 & -1 & 1 & -1 \\ 1 & 1 & -1 & -1 \end{pmatrix} \cdot \begin{pmatrix} \pm \cos \theta_1 \\ \pm \cos \theta_2 \\ \pm \cos \theta_3 \\ \pm \cos \theta_4 \end{pmatrix} \quad (\text{A7})$$

Because of the ambiguity in $\pm \cos \theta$, we have 2^4 possible solutions \hat{b} . However, most of these solutions represent four cones that are not oriented correctly. Unwanted solutions will have a large sum of squared residuals [57]

$$S(\hat{b}) = (c - N\hat{b})^T (c - N\hat{b}), \quad (\text{A8})$$

meaning we can compute $S(\hat{b})$ and choose the vector \hat{b} that minimizes S .

Finally, the resulting vector \vec{B} can only be determined up to a symmetry of T_d , stemming from the tetrahedral structure of the diamond lattice. One can circumvent this restriction with a known bias field, which breaks the symmetry of the problem. After determining the direction of the bias field using a known external magnetic field, changes in the magnetic field that are small compared to the bias field can be vectorially resolved without ambiguities. The resulting magnetic field vector still has to be transferred from NV coordinates to outer lab coordinates. This can also be accomplished with a known bias field because the unknown orientation of the diamond on the fiber tip can be obtained from one calibration measurement of the known bias field.

Appendix B: Sensitivity optimizations

Optimizing all eight ODMR resonances for their best sensitivity simultaneously is generally not possible. Due to imperfect optical and MW addressing, each resonance will have a slightly different contrast and linewidth and, therefore, a different set of optimal measurement parameters, especially when one changes

laser power, MW power, MW modulation frequency, or MW modulation deviation. FIG. 8 shows, as an example, the dependence of the LIA signal slope on the MW modulation frequency and deviation.

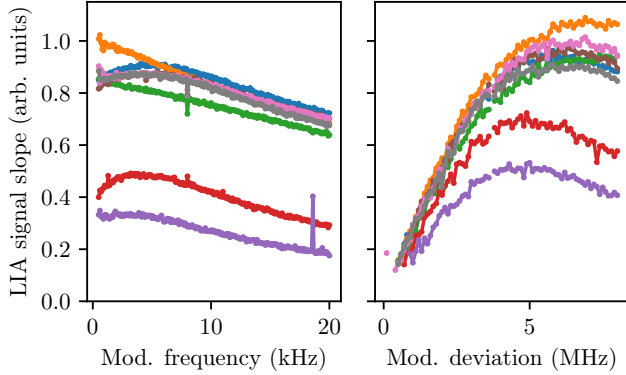


FIG. 8. Zero-crossing slope of the LIA output for all eight resonances dependent on MW modulation frequency (left) and modulation deviation (right), each color representing one resonance. Each resonance generally has a different set of parameters where the zero-crossing slope and, therefore, the magnetic field sensitivity is maximized.

This leads to the fact that each resonance has its own sensitivity. Table I lists our achieved sensitivities for each resonance of the ODMR spectrum shown in FIG. 4 and 5.

TABLE I. Magnetic field sensitivities for each resonance

Nr.	η_{LIA}	$\eta_{SN,MM}$	$\eta_{SN,SM,MM}$
1	60.0 nT/ $\sqrt{\text{Hz}}$	6.14 nT/ $\sqrt{\text{Hz}}$	30.0 nT/ $\sqrt{\text{Hz}}$
2	53.8 nT/ $\sqrt{\text{Hz}}$	5.90 nT/ $\sqrt{\text{Hz}}$	30.5 nT/ $\sqrt{\text{Hz}}$
3	60.9 nT/ $\sqrt{\text{Hz}}$	9.89 nT/ $\sqrt{\text{Hz}}$	48.2 nT/ $\sqrt{\text{Hz}}$
4	70.4 nT/ $\sqrt{\text{Hz}}$	7.95 nT/ $\sqrt{\text{Hz}}$	29.7 nT/ $\sqrt{\text{Hz}}$
5	77.2 nT/ $\sqrt{\text{Hz}}$	9.70 nT/ $\sqrt{\text{Hz}}$	33.9 nT/ $\sqrt{\text{Hz}}$
6	51.8 nT/ $\sqrt{\text{Hz}}$	8.17 nT/ $\sqrt{\text{Hz}}$	40.9 nT/ $\sqrt{\text{Hz}}$
7	57.5 nT/ $\sqrt{\text{Hz}}$	6.34 nT/ $\sqrt{\text{Hz}}$	30.1 nT/ $\sqrt{\text{Hz}}$
8	59.2 nT/ $\sqrt{\text{Hz}}$	6.50 nT/ $\sqrt{\text{Hz}}$	27.7 nT/ $\sqrt{\text{Hz}}$

Appendix C: Geometrical design of the polymer structure

A schematic image of the designed polymer waveguide structure is shown in FIG. 9. The base of the cone

has a diameter of ($d_1 = 55 \mu\text{m}$) and is slightly larger than the $50 \mu\text{m}$ sized core of the mm fiber having ($5 \mu\text{m}$) of positional tolerance and slightly increasing the adhesion between polymer structure and optical fiber. Furthermore, the cone stands on top of a $h_1 = 5 \mu\text{m}$ tall cylinder. The tip of the cone is designed to be slightly larger ($d_2 = 30 \mu\text{m}$) than the diameter of the $15 \mu\text{m}$ sized diamond. The edges of the tip of the cone are also rounded to reduce physical contact with the glass substrate below, as shown in the image. The total height h_3 is $50 \mu\text{m}$. Due to scattering of the laser beam in the center of the cone caused by the microdiamond during the direct laser writing process, the structure is written in 12 contour-lines with $0.4 \mu\text{m}$ spacing in between and a top layer thickness below and around the diamond of only ($12 \mu\text{m}$). A second polymer structure connecting a single-mode (SM) fiber to the diamond for an additional optical excitation guiding beam path is added. The waveguide structure consists of a small cone with a base diameter of ($d_5 = 20 \mu\text{m}$) and height of $5 \mu\text{m}$ at which the cone diameter is $d_3 = 10 \mu\text{m}$. The initial $10 \mu\text{m}$ wide waveguide follows a 90° curve with a $r_1 = 28 \mu\text{m}$ radius a straight line with a length of $l_2 = 88 \mu\text{m}$ and is then guided lightly upwards at a $r_2 = 30 \mu\text{m}$ radius which then guides light centrally at the designed diamond center position. At this position, the waveguide has a width of $d_3 = 12 \mu\text{m}$, which is increased gradually. The waveguide structure is supported via two small towers and intentionally designed such that it does not bond to the glass substrate, which is at the same height as the diamond. Further geometrical values are $h_2 = 37 \mu\text{m}$ and $l_2 = 150 \mu\text{m}$.

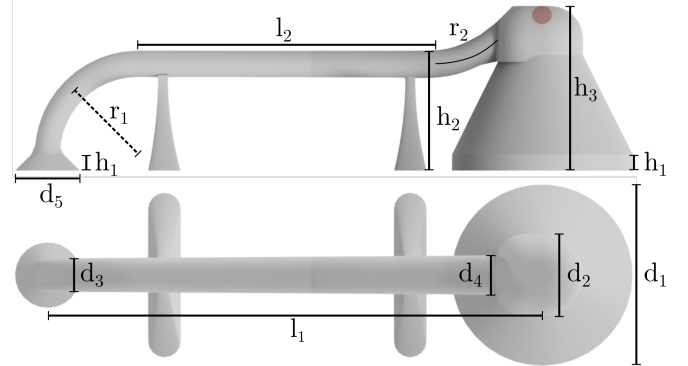


FIG. 9. Schematic rendering of the designed polymer structure and given geometries. The red dot indicates the intended position of the microdiamond.

[1] J. H. N. Loubser and J. A. V. Wyk, Electron spin resonance in the study of diamond, *Reports on Progress in Physics* **41**, 1201 (1978).

[2] M. W. Doherty, N. B. Manson, P. Delaney, F. Jelezko, J. Wrachtrup, and L. C. Hollenberg, The nitrogen-vacancy colour centre in diamond, *Physics Reports* **528**, 1 (2013).

- [3] L. Rondin, J.-P. Tetienne, T. Hingant, J.-F. Roch, P. Maletinsky, and V. Jacques, Magnetometry with nitrogen-vacancy defects in diamond, *Reports on Progress in Physics* **77**, 056503 (2014).
- [4] E. V. Levine, M. J. Turner, P. Kehayias, C. A. Hart, N. Langellier, R. Trubko, D. R. Glenn, R. R. Fu, and R. L. Walsworth, Principles and techniques of the quantum diamond microscope, *Nanophotonics* **8**, 1945 (2019).
- [5] A. Haque and S. Sumaiya, An Overview on the Formation and Processing of Nitrogen-Vacancy Photonic Centers in Diamond by Ion Implantation, *Journal of Manufacturing and Materials Processing* **1**, 6 (2017).
- [6] J. F. Barry, M. H. Steinecker, S. T. Alsid, J. Majumder, L. M. Pham, M. F. O'Keefe, and D. A. Braje, Sensitive AC and DC Magnetometry with Nitrogen-Vacancy Center Ensembles in Diamond (2023), arXiv:2305.06269.
- [7] V. M. Acosta, E. Bauch, M. P. Ledbetter, A. Waxman, L.-S. Bouchard, and D. Budker, Temperature Dependence of the Nitrogen-Vacancy Magnetic Resonance in Diamond, *Physical Review Letters* **104**, 070801 (2010).
- [8] S. Choe, J. Yoon, M. Lee, J. Oh, D. Lee, H. Kang, C.-H. Lee, and D. Lee, Precise temperature sensing with nanoscale thermal sensors based on diamond NV centers, *Current Applied Physics* **18**, 1066 (2018).
- [9] P. Kehayias, M. J. Turner, R. Trubko, J. M. Schloss, C. A. Hart, M. Wesson, D. R. Glenn, and R. L. Walsworth, Imaging crystal stress in diamond using ensembles of nitrogen-vacancy centers, *Physical Review B* **100**, 174103 (2019).
- [10] F. Dolde, H. Fedder, M. W. Doherty, T. Nöbauer, F. Rempp, G. Balasubramanian, T. Wolf, F. Reinhard, L. C. L. Hollenberg, F. Jelezko, and J. Wrachtrup, Electric-field sensing using single diamond spins, *Nature Physics* **7**, 459 (2011).
- [11] E. Van Oort and M. Glasbeek, Electric-field-induced modulation of spin echoes of N-V centers in diamond, *Chemical Physics Letters* **168**, 529 (1990).
- [12] P. Tamarat, T. Gaebel, J. R. Rabeau, M. Khan, A. D. Greentree, H. Wilson, L. C. L. Hollenberg, S. Praver, P. Hemmer, F. Jelezko, and J. Wrachtrup, Stark Shift Control of Single Optical Centers in Diamond, *Physical Review Letters* **97**, 083002 (2006).
- [13] J.-P. Tetienne, N. Dontschuk, D. A. Broadway, A. Stacey, D. A. Simpson, and L. C. L. Hollenberg, Quantum imaging of current flow in graphene, *Science Advances* **3**, e1602429 (2017).
- [14] J.-H. Storm, P. Hömmen, D. Drung, and R. Körber, An ultra-sensitive and wideband magnetometer based on a superconducting quantum interference device, *Applied Physics Letters* **110**, 072603 (2017).
- [15] W. C. Griffith, S. Knappe, and J. Kitching, Femtotesla atomic magnetometry in a microfabricated vapor cell, *Optics Express* **18**, 27167 (2010).
- [16] S. C. Scholten, A. J. Healey, I. O. Robertson, G. J. Abrahams, D. A. Broadway, and J.-P. Tetienne, Widefield quantum microscopy with nitrogen-vacancy centers in diamond: Strengths, limitations, and prospects, *Journal of Applied Physics* **130**, 150902 (2021).
- [17] Y. Hatano, J. Shin, J. Tanigawa, Y. Shigenobu, A. Nakazono, T. Sekiguchi, S. Onoda, T. Ohshima, K. Arai, T. Iwasaki, and M. Hatano, High-precision robust monitoring of charge/discharge current over a wide dynamic range for electric vehicle batteries using diamond quantum sensors, *Scientific Reports* **12**, 13991 (2022).
- [18] D. A. Broadway, S. C. Scholten, C. Tan, N. Dontschuk, S. E. Lillie, B. C. Johnson, G. Zheng, Z. Wang, A. R. Oganov, S. Tian, C. Li, H. Lei, L. Wang, L. C. L. Hollenberg, and J. Tetienne, Imaging Domain Reversal in an Ultrathin Van der Waals Ferromagnet, *Advanced Materials* **32**, 2003314 (2020).
- [19] S. Steinert, F. Ziem, L. T. Hall, A. Zappe, M. Schweikert, N. Götz, A. Aird, G. Balasubramanian, L. Hollenberg, and J. Wrachtrup, Magnetic spin imaging under ambient conditions with sub-cellular resolution, *Nature Communications* **4**, 1607 (2013).
- [20] C. Degen, Microscopy with single spins, *Nature Nanotechnology* **3**, 643 (2008).
- [21] P. Rembold, N. Oshnik, M. M. Müller, S. Montangero, T. Calarco, and E. Neu, Introduction to quantum optimal control for quantum sensing with nitrogen-vacancy centers in diamond, *AVS Quantum Science* **2**, 024701 (2020).
- [22] E. O. Schäfer-Nolte, *Development of a diamond-based scanning probe spin sensor operating at low temperature in ultra high vacuum*, Ph.D. thesis, Universität Stuttgart (2014).
- [23] T. Wolf, P. Neumann, K. Nakamura, H. Sumiya, T. Ohshima, J. Isoya, and J. Wrachtrup, Subpicotesla Diamond Magnetometry, *Physical Review X* **5**, 041001 (2015).
- [24] J. H. Shim, S.-J. Lee, S. Ghimire, J. I. Hwang, K.-G. Lee, K. Kim, M. J. Turner, C. A. Hart, R. L. Walsworth, and S. Oh, Multiplexed Sensing of Magnetic Field and Temperature in Real Time Using a Nitrogen-Vacancy Ensemble in Diamond, *Physical Review Applied* **17**, 014009 (2022).
- [25] K. Kubota, Y. Hatano, Y. Kainuma, J. Shin, D. Nishitani, C. Shinei, T. Taniguchi, T. Teraji, S. Onoda, T. Ohshima, T. Iwasaki, and M. Hatano, Wide temperature operation of diamond quantum sensor for electric vehicle battery monitoring, *Diamond and Related Materials* **135**, 109853 (2023).
- [26] P. J. Scheidegger, S. Diesch, M. L. Palm, and C. L. Degen, Scanning nitrogen-vacancy magnetometry down to 350 mK, *Applied Physics Letters* **120**, 224001 (2022).
- [27] G.-Q. Liu, X. Feng, N. Wang, Q. Li, and R.-B. Liu, Coherent quantum control of nitrogen-vacancy center spins near 1000 kelvin, *Nature Communications* **10**, 1344 (2019).
- [28] G. J. Abrahams, S. C. Scholten, A. J. Healey, I. O. Robertson, N. Dontschuk, S. Q. Lim, B. C. Johnson, D. A. Simpson, L. C. L. Hollenberg, and J.-P. Tetienne, An integrated widefield probe for practical diamond nitrogen-vacancy microscopy, *Applied Physics Letters* **119**, 254002 (2021).
- [29] P. Appel, E. Neu, M. Ganzhorn, A. Barfuss, M. Batzer, M. Gratz, A. Tschöpe, and P. Maletinsky, Fabrication of all diamond scanning probes for nanoscale magnetometry, *Review of Scientific Instruments* **87**, 063703 (2016).
- [30] J. L. Webb, J. D. Clement, L. Troise, S. Ahmadi, G. J. Johansen, A. Huck, and U. L. Andersen, Nanotesla sensitivity magnetic field sensing using a compact diamond nitrogen-vacancy magnetometer,

- [Applied Physics Letters](#) **114**, 231103 (2019).
- [31] D. Zheng, Z. Ma, W. Guo, L. Niu, J. Wang, X. Chai, Y. Li, Y. Sugawara, C. Yu, Y. Shi, X. Zhang, J. Tang, H. Guo, and J. Liu, A hand-held magnetometer based on an ensemble of nitrogen-vacancy centers in diamond, [Journal of Physics D: Applied Physics](#) **53**, 155004 (2020).
- [32] F. M. Stürner, A. Brenneis, J. Kassel, U. Wostradowski, R. Rölver, T. Fuchs, K. Nakamura, H. Sumiya, S. Onoda, J. Isoya, and F. Jelezko, Compact integrated magnetometer based on nitrogen-vacancy centres in diamond, [Diamond and Related Materials](#) **93**, 59 (2019).
- [33] J. Pogorzelski, L. Horsthemke, J. Homrighausen, D. Stiegekötter, M. Gregor, and P. Glösekötter, Compact and Fully Integrated LED Quantum Sensor Based on NV Centers in Diamond, [Sensors](#) **24**, 743 (2024).
- [34] R. Patel, L. Zhou, A. Frangeskou, G. Stimpson, B. Breeze, A. Nikitin, M. Dale, E. Nichols, W. Thornley, B. Green, M. Newton, A. Edmonds, M. Markham, D. Twitchen, and G. Morley, Subnanotesla Magnetometry with a Fiber-Coupled Diamond Sensor, [Physical Review Applied](#) **14**, 044058 (2020).
- [35] A. Kuwahata, T. Kitaizumi, K. Saichi, T. Sato, R. Igarashi, T. Ohshima, Y. Masuyama, T. Iwasaki, M. Hatano, F. Jelezko, M. Kusakabe, T. Yatsui, and M. Sekino, Magnetometer with nitrogen-vacancy center in a bulk diamond for detecting magnetic nanoparticles in biomedical applications, [Scientific Reports](#) **10**, 2483 (2020).
- [36] F. M. Stürner, A. Brenneis, T. Buck, J. Kassel, R. Rölver, T. Fuchs, A. Savitsky, D. Suter, J. Grimm, S. Hengesbach, M. Förtsch, K. Nakamura, H. Sumiya, S. Onoda, J. Isoya, and F. Jelezko, Integrated and Portable Magnetometer Based on Nitrogen-Vacancy Ensembles in Diamond, [Advanced Quantum Technologies](#) **4**, 2000111 (2021).
- [37] D. Kim, M. I. Ibrahim, C. Foy, M. E. Trusheim, R. Han, and D. R. Englund, A CMOS-integrated quantum sensor based on nitrogen-vacancy centres, [Nature Electronics](#) **2**, 284 (2019).
- [38] M. Zhao, Q. Lin, Q. Meng, W. Shan, L. Zhu, Y. Chen, T. Liu, L. Zhao, and Z. Jiang, All Fiber Vector Magnetometer Based on Nitrogen-Vacancy Center, [Nanomaterials](#) **13**, 949 (2023).
- [39] S. Dix, J. Gutsche, E. Waller, G. Von Freymann, and A. Widera, Fiber-tip endoscope for optical and microwave control, [Review of Scientific Instruments](#) **93**, 095104 (2022).
- [40] M. Bianco, A. Balena, M. Pisanello, F. Pisano, L. Sileo, B. Spagnolo, C. Montinaro, B. L. Sabatini, M. D. Vittorio, and F. Pisanello, Comparative study of autofluorescence in flat and tapered optical fibers towards application in depth-resolved fluorescence lifetime photometry in brain tissue, [Biomedical Optics Express](#) **12**, 993 (2021).
- [41] J. A. Udovich, N. D. Kirkpatrick, A. Kano, A. West Rynes, U. Utzinger, and A. F. Gmitro, Spectral background and transmission characteristics of fiber optic imaging bundles, [Applied Optics](#) **47**, 4560 (2008).
- [42] E. H. Waller, S. Dix, J. Gutsche, A. Widera, and G. V. Freymann, Functional Metallic Microcomponents via Liquid-Phase Multiphoton Direct Laser Writing: A Review, [Micromachines](#) **10**, 827 (2019).
- [43] M. Schmid, D. Ludescher, and H. Giessen, Optical properties of photoresists for femtosecond 3D printing: refractive index, extinction, luminescence-dose dependence, aging, heat treatment and comparison between 1-photon and 2-photon exposure, [Optical Materials Express](#) **9**, 4564 (2019).
- [44] J. L. Sánchez Toural, V. Marzoa, R. Bernardo-Gavito, J. L. Pau, and D. Granados, Hands-On Quantum Sensing with NV-Centers in Diamonds, [C](#) **9**, 16 (2023).
- [45] J. J. Moré, The Levenberg-Marquardt algorithm: Implementation and theory, in [Numerical Analysis](#), Vol. 630, edited by G. A. Watson (Springer Berlin Heidelberg, Berlin, Heidelberg, 1978) pp. 105–116, series Title: Lecture Notes in Mathematics.
- [46] J. M. Schloss, J. F. Barry, M. J. Turner, and R. L. Walsworth, Simultaneous Broadband Vector Magnetometry Using Solid-State Spins, [Physical Review Applied](#) **10**, 034044 (2018).
- [47] A. Dréau, M. Lesik, L. Rondin, P. Spinicelli, O. Arcizet, J.-F. Roch, and V. Jacques, Avoiding power broadening in optically detected magnetic resonance of single NV defects for enhanced dc magnetic field sensitivity, [Physical Review B](#) **84**, 195204 (2011).
- [48] N. Sekiguchi, M. Fushimi, A. Yoshimura, C. Shinei, M. Miyakawa, T. Taniguchi, T. Teraji, H. Abe, S. Onoda, T. Ohshima, M. Hatano, M. Sekino, and T. Iwasaki, Diamond quantum magnetometer with dc sensitivity of $< 10 \text{ pT Hz}^{-1/2}$ toward measurement of biomagnetic field (2023), [arXiv:2309.04093](#).
- [49] S. Ahmadi, H. A. R. El-Ella, J. O. B. Hansen, A. Huck, and U. L. Andersen, Pump-Enhanced Continuous-Wave Magnetometry Using Nitrogen-Vacancy Ensembles, [Physical Review Applied](#) **8**, 034001 (2017).
- [50] D. Allan, Statistics of atomic frequency standards, [Proceedings of the IEEE](#) **54**, 221 (1966).
- [51] D. A. Van Baak and G. Herold, Response of a lock-in amplifier to noise, [American Journal of Physics](#) **82**, 785 (2014).
- [52] J. Zhang, T. Liu, L. Xu, G. Bian, P. Fan, M. Li, C. Xu, and H. Yuan, A pulsed lock-in method for DC ensemble nitrogen-vacancy center magnetometry, [Diamond and Related Materials](#) **125**, 109035 (2022).
- [53] M. S. Dix, D. Lönard, I. Cardoso Barbosa, J. Gutsche, J. Witzernath, and A. Widera, Data for A miniaturized magnetic field sensor based on nitrogen-vacancy centers, [10.5281/zenodo.10849545](#) (2024).
- [54] [Microscope Experiment Control Application](#) (2024).
- [55] G. Balasubramanian, I. Y. Chan, R. Kolesov, M. Al-Hmoud, J. Tisler, C. Shin, C. Kim, A. Wojcik, P. R. Hemmer, A. Krueger, T. Hanke, A. Leitenstorfer, R. Bratschitsch, F. Jelezko, and J. Wrachtrup, Nanoscale imaging magnetometry with diamond spins under ambient conditions, [Nature](#) **455**, 648 (2008).
- [56] Y. Wang, R. Zhang, Y. Yang, Q. Wu, Z. Yu, and B. Chen, Orientation determination of nitrogen-vacancy center in diamond using a static magnetic field, [Chinese Physics B](#) **32**, 070301 (2023).
- [57] W. H. Press, S. A. Teukolsky, W. T. Vetterling, and B. P. Flannery, [Numerical Recipes - The Art of Scientific Computing - 3rd Edition](#) (Cambridge University Press, 2007).